nature geoscience

ARTICLES

https://doi.org/10.1038/s41561-020-0584-3

Check for updates

# Chesapeake Bay acidification buffered by spatially decoupled carbonate mineral cycling

Jianzhong Su[1,2], Wei-Jun Cai[1]✉, Jean Brodeur[1], Baoshan Chen[1], Najid Hussain[1], Yichen Yao[3], Chaoying Ni[3], Jeremy M. Testa[4], Ming Li[5], Xiaohui Xie[5,8], Wenfei Ni[5], K. Michael Scaboo[1], Yuan-yuan Xu[1], Jeffrey Cornwell[5], Cassie Gurbisz[6], Michael S. Owens[5], George G. Waldbusser[7], Minhan Dai[2] and W. Michael Kemp[5]

**Uptake of anthropogenic carbon dioxide ($CO_2$) from the atmosphere has acidified the ocean and threatened the health of marine organisms and their ecosystems. In coastal waters, acidification is often enhanced by $CO_2$ and acids produced under high rates of biological respiration. However, less is known about buffering processes that counter coastal acidification in eutrophic and seasonally hypoxic water bodies, such as the Chesapeake Bay. Here, we use carbonate chemistry, mineralogical analyses and geochemical modelling to demonstrate the occurrence of a bay-wide pH-buffering mechanism resulting from spatially decoupled calcium carbonate mineral cycling. In summer, high rates of photosynthesis by dense submerged aquatic vegetation at the head of the bay and in shallow, nearshore areas generate high pH, an elevated carbonate mineral saturation state and net alkalinity uptake. Calcium carbonate particles produced under these conditions are subsequently transported downstream into corrosive subsurface waters, where their dissolution buffers pH decreases caused by aerobic respiration and anthropogenic $CO_2$. Because this pH-buffering mechanism would be strengthened by further nutrient load reductions and associated submerged aquatic vegetation recovery, our findings suggest that the reduction of nutrient inputs into coastal waters will not only reduce eutrophication and hypoxia, but also alleviate the severity of coastal ocean acidification.**

Since the industrial revolution, the global ocean has absorbed approximately 30% of the anthropogenic $CO_2$ emissions from the atmosphere, lowering the average surface ocean water pH by 0.1 units and aragonite carbonate mineral saturation state ($\Omega_{arag}$) by 0.5 units. This process, known as ocean acidification[1,2], is harmful to some marine organisms and ecosystems[3]. In coastal waters, acidification is enhanced by eutrophication and the subsequent hypoxia and anoxia via the accumulation of $CO_2$ and acids below the pycnocline[4,5]. Calcium carbonate ($CaCO_3$) mineral dissolution can increase the total alkalinity (TA) of water, and is proposed as a buffer to neutralize anthropogenic $CO_2$ uptake[6,7]. Recent studies have shown that $CaCO_3$ dissolution can offset a notable proportion of the metabolic $CO_2$ and increase survivorship of juvenile bivalves, thus providing a substantial negative feedback to coastal acidification[8,9].

However, very few studies have linked $CaCO_3$ dissolution to the timing and location of its formation in coastal waters[10,11] as a corollary to the ocean's carbonate counter pump[11]. These dynamic links are essential to understand given their capacity to mediate aquatic pH and atmospheric $CO_2$ concentrations[8,12]. In coastal waters, $CaCO_3$ can be formed via abiotic precipitation or biotic production, which are usually associated with coral reefs, calcareous algae[13], molluscs[14], bacteria[15], fish[16] and aquatic plants[17]. Recently, seagrass meadows have been shown to be major sites for $CaCO_3$ accumulation and storage in high-salinity waters in equatorial and subtropical regions[18]. In addition to calcification from the seagrass-calcifying algae, infauna and epibiont community, the seagrass *Thalassia testudinum* itself can accumulate aragonite crystals within its cell walls and externally on the blade surface through biologically induced precipitation[19]. High-pH and -$\Omega_{arag}$ conditions will also favour biogenic shell formation. As pH is generally very high and the partial pressure of $CO_2$ ($p_{CO_2}$) is very low in these systems during daytime hours, the $CO_2$ released as a by-product of $CaCO_3$ precipitation should be utilized by aquatic plant biomass production and not released to the atmosphere. Once the $CaCO_3$ crystals escape out of the seagrass beds[20,21], they can be transported to carbonate-undersaturated areas where they can dissolve, reduce the concentration of $H^+$ and increase alkalinity and $\Omega_{arag}$.

Anthropogenic perturbations have altered the distribution, abundance and diversity of submerged aquatic vegetation (SAV) on the shoals of the Chesapeake Bay and its tributaries[22,23]. A bay-wide decline of SAV began in the 1960s, accelerated in the early 1970s and continued through the 1980s. Restoring these once-abundant SAV beds has been a primary goal of efforts to reduce loads of nutrients and sediments to the estuary[24,25]. Lefcheck et al.[25] demonstrated that bay-wide water column nitrogen concentrations have declined by 23%, coinciding with a 316% increase in SAV cover from 1984 to 2015. Note that nutrient loads are still sufficiently high that surface water phytoplankton blooms and subsequent subsurface water hypoxia remain a serious issue along the main channel[26–28]. Although SAV populations remain well below restoration targets in some meso- and polyhaline regions, there have been widespread resurgences throughout the tidal fresh and oligohaline portions of the

[1]School of Marine Science and Policy, University of Delaware, Newark, DE, USA. [2]State Key Laboratory of Marine Environmental Science, Xiamen University, Xiamen, China. [3]Materials Science and Engineering, University of Delaware, Newark, DE, USA. [4]Chesapeake Biological Laboratory, University of Maryland Center for Environmental Science, Solomons, MD, USA. [5]Horn Point Laboratory, University of Maryland Center for Environmental Science, Cambridge, MD, USA. [6]St. Mary's College of Maryland, St. Mary's City, MD, USA. [7]College of Earth, Ocean, and Atmospheric Sciences, Oregon State University, Corvallis, OR, USA. [8]Present address: State Key Laboratory of Satellite Ocean Environment Dynamics, Second Institute of Oceanography, Hangzhou, China. ✉e-mail: wcai@udel.edu

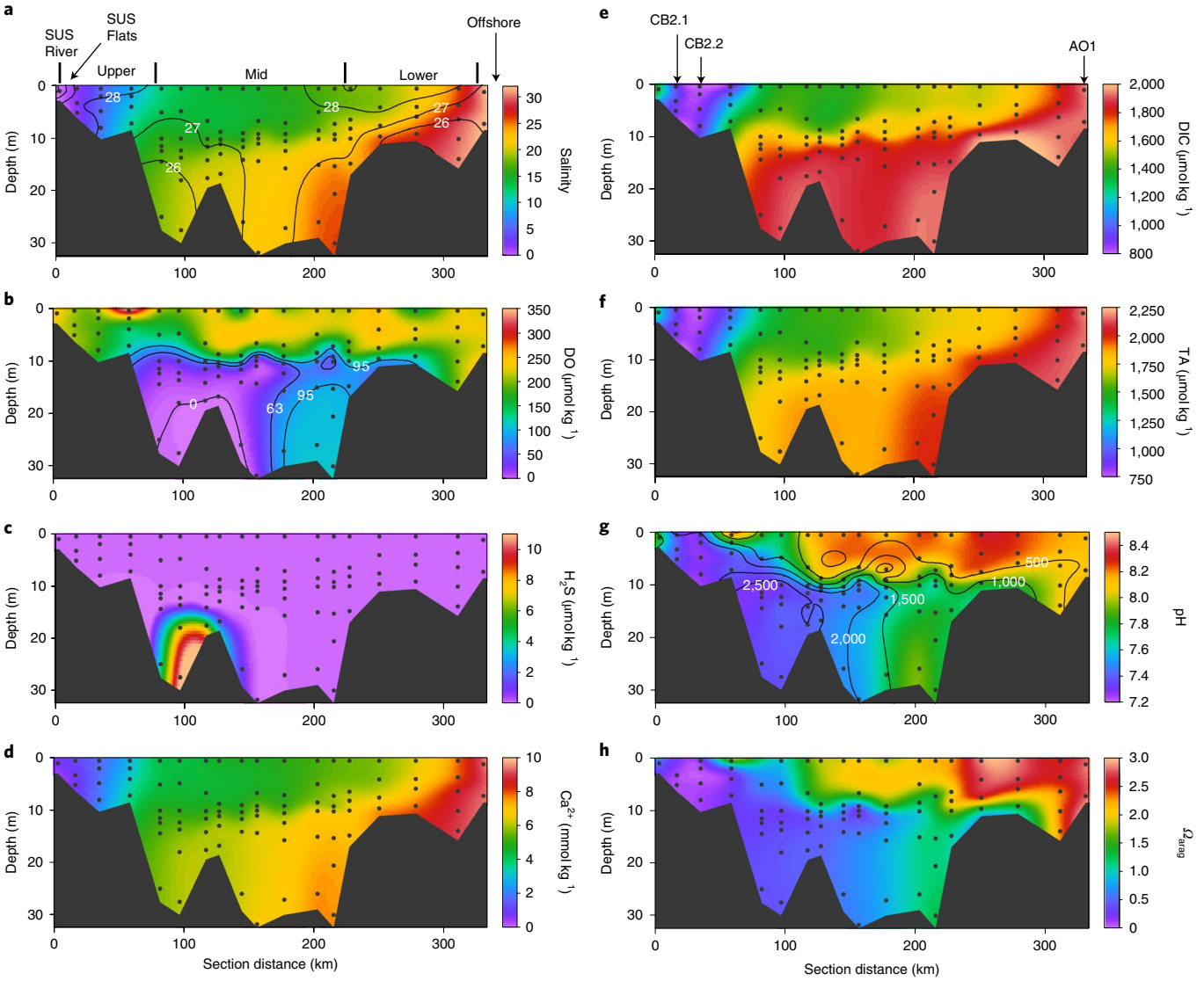


**Fig. 1 | Distributions of water properties in the Chesapeake Bay in August 2016. a–h**, Salinity (colour scale) and contours of temperature (°C) (**a**), dissolved oxygen (DO; colour scale) and contours for anoxia (0 μmol kg$^{-1}$) and hypoxia (<63 μmol kg$^{-1}$) (**b**), hydrogen sulfide concentration (**c**), calcium ion concentration (**d**), DIC (**e**), TA (**f**), pH (colour scale) and contours for $p_{CO_2}$ (μatm) (**g**) and $\Omega_{arag}$ (**h**) along the main channel. The mainstem bay was separated into three regions (that is, upper bay, mid bay and lower bay[26]). See Extended Data Fig. 1 for a station map. Black dots represent sampling stations and depths. SUS, Susquehanna.

mainstem bay and its tributaries over the past decade[23]. One of the largest recovered SAV beds lies in the Susquehanna Flats—a broad, tidal freshwater region located near the mouth of the Susquehanna River at the head of the bay. The SAV in the flats was sparse through much of the 1980s and 1990s and then recovered rapidly in size and density between 2000 and 2006, and remained persistently large and dense after 2007[29].

To understand how a large estuary responds to the dual stresses of eutrophication and acidification, we examined the spatial and temporal distribution of carbonate chemistry and derived the patterns of $CaCO_3$ formation and dissolution in the Chesapeake Bay in August 2016, at a time of peak hypoxia, anoxia and SAV biomass (Extended Data Fig. 1). Supplementary cruises were conducted in the Susquehanna Flats to collect surface sediments and SAV leaves for mineralogical identification, and to verify TA removal inside the flats. The Chesapeake Bay is an ideal system to examine these $CaCO_3$ dynamics because it suffers from hypoxia-/anoxia-enhanced acidification and associated bottom water $CaCO_3$ dissolution[8,26,27,30,31], but also supports a productive shellfish industry[32] and a diverse assemblage of SAV[25].

## Calcium carbonate formation in the upper Chesapeake Bay

In summer, strong gradients of salinity and temperature contributed to the formation of vertical stratification, facilitating the occurrence of hypoxia and anoxia below the pycnocline in the mid bay (Fig. 1a–c). The distribution of calcium ion ($Ca^{2+}$), dissolved inorganic carbon (DIC) and TA generally resembled the pattern of salinity (that is, increasing seaward and from the surface to the bottom) (Fig. 1d–f). However, there were also differences among DIC, TA and salinity, suggesting non-conservative removal or addition. In particular, DIC and TA in the upper bay were distinctly lower than in the Susquehanna River. The pH and $\Omega_{arag}$ were low in the upper bay, and gradually increased seaward below the pycnocline, whereas those in surface waters more rapidly increased seaward (Fig. 1g,h). The $p_{CO_2}$ was high in the upper bay and in subsurface waters in hypoxic and anoxic zones (Fig. 1g).

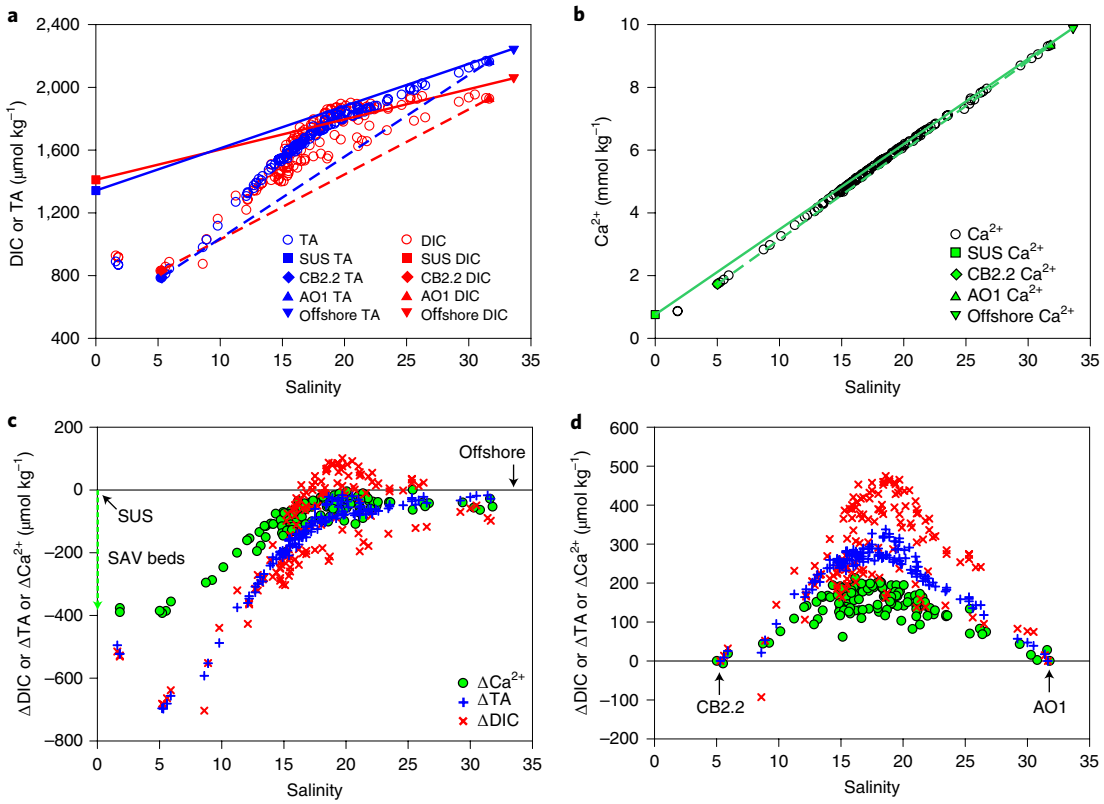


**Fig. 2 | Non-conservative carbonate system behaviour. a**,**b**, DIC and TA (**a**) and calcium ion concentration (**b**) (all open symbols) are plotted against salinity, while endmember values (filled symbols) represent the measurements for specific water masses at these endmembers. **c**, Deviation from conservative mixing (solid lines in **a** and **b**) between Susquehanna River water and offshore seawater, illustrating the accumulated removal or addition across the entire bay. Note that there is a zero reference line and the endmembers are marked by arrows. **d**, Deviation values relative to conservative mixing between stations CB2.2 and AO1 (dashed lines in **a** and **b**), illustrating $CaCO_3$ dissolution.

To evaluate the carbonate dynamics over a bay-wide scale, we applied a two-endmember mixing scheme between Susquehanna River water and offshore seawater (Fig. 2a,b). We found a large deficit, and thus a drawdown, of $Ca^{2+}$ and TA in the upper bay (Fig. 2c). The removals of $Ca^{2+}$ and TA reached peak values of 393 and 698 μmol $kg^{-1}$, respectively, at a salinity of <5, then decreased to 53 and 28 μmol $kg^{-1}$ at a high salinity of 31.7. Since the signals of removal or addition are cumulative along the salinity gradient in an estuary[33], we surmise that $Ca^{2+}$ was scavenged near the freshwater area. As we lacked samples inside the SAV beds in the freshwater region in the August 2016 cruise and during the sensor deployment period (summer to autumn 2016), additional samples were collected within the Susquehanna Flats in early September 2018. The maximum removals of $Ca^{2+}$ and TA in 2018 within this SAV bed relative to the river mouth reached up to 285 and 450 μmol $kg^{-1}$ (Extended Data Fig. 2d), respectively, which are close to the lower end of calculated $Ca^{2+}$ and TA removals at station CB2.1 (318 and 388 μmol $kg^{-1}$) during August 2016. Note that for $CaCO_3$ precipitation, the known stoichiometry ratio of DIC and TA changes should be 1:2. However, the nearly 1:1 ratio downstream of the flats at stations CB2.1 and CB2.2 reflects contributions from other processes, such as $CO_2$ outgassing and sediment–water exchange (Fig. 2c). Details on the evolution of $Ca^{2+}$, TA and DIC at sites CB2.1 and CB2.2 are provided in the Methods and Supplementary Fig. 1. As salinity increased (salinity >5) in the mid to lower bay, the local $Ca^{2+}$ addition began to exceed $Ca^{2+}$ removal, which gradually compensated the removal signal to a large extent.

We postulate that the large $Ca^{2+}$ and TA removal near the freshwater zone is attributed to $CaCO_3$ formation within the Susquehanna Flats SAV bed. Three additional lines of evidence support this postulation. First, continuous monitoring sensor data showed very high dissolved oxygen saturation (DO%) and pH inside the SAV beds during summer and autumn seasons in 2016 (Fig. 3a), indicating that high photosynthesis within SAV beds created favourable $\Omega$ for $CaCO_3$ formation. For instance, in August 2016, the monthly average DO% and pH were 124 ± 24% and 9.7 ± 0.2, with the highest values exceeding 179% for DO% and 10.1 for pH. The water column $\Omega_{arag}$ calculated from TA and DIC was highly supersaturated (14.3) despite low concentrations of $Ca^{2+}$ inside the SAV beds in September 2018. Previous studies had demonstrated that photosynthesis could enhance biogenic calcification, because of the shift in the carbonate system by $CO_2$ removal and pH increase[13,34,35]. Furthermore, the diffusive boundary layer immediately adjacent to the leaves within the beds could probably generate microzones with even higher pH and $\Omega_{arag}$, where photosynthesis-induced $CaCO_3$ precipitation may quickly occur[36].

Second, scanning electron microscopy (SEM) images illustrated $CaCO_3$ precipitation with varying size and morphology on the leaf surface of *Vallisneria americana* (Fig. 3b), which is a dominant species in the SAV beds[29]. Most $CaCO_3$ solids were in the order of several hundred nanometres, but sometimes were several micrometres long or even larger by aggregating with other materials, such as fine-grained minerals, organic mucus and diatom fragments (Extended Data Fig. 3). The atomic composition of the rice-like $CaCO_3$ aggregates (41.6% O; 38.1% Ca; 12.5% C) is very close to that of pure $CaCO_3$ crystals (48% O; 40% Ca; 12% C).

Third, the average $CaCO_3$ content in the SAV leaf samples (5.66 ± 4.31%) was 25 times more than that in the surface sediment samples (0.22 ± 0.16%) in late summer. Since the epiphyte shells

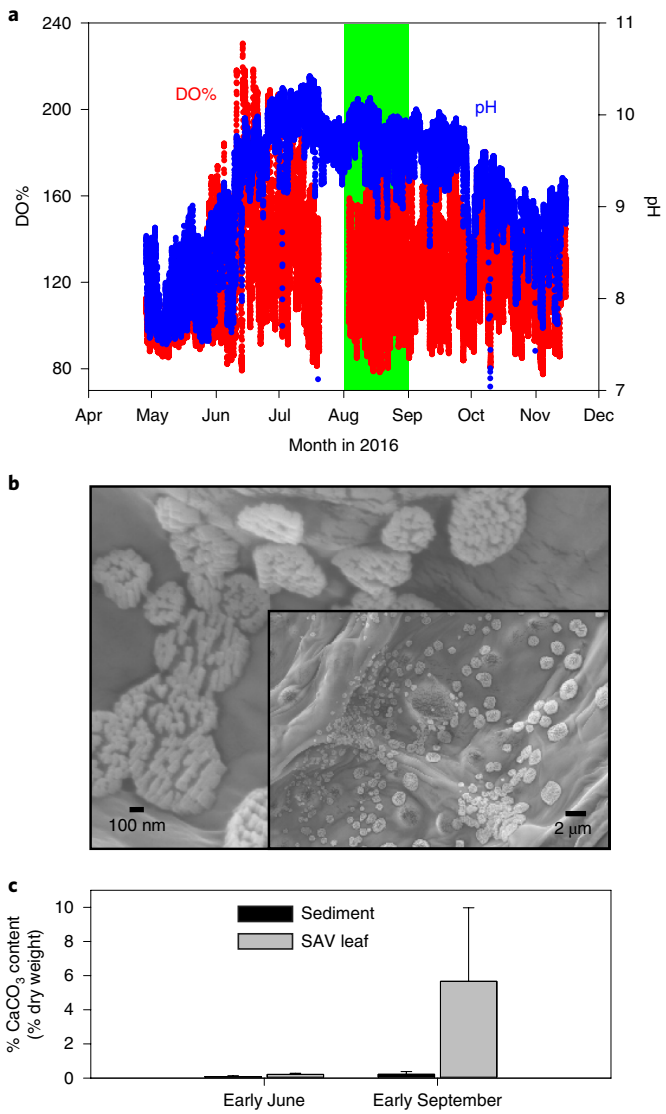


**Fig. 3 | Water chemistry and calcium carbonate precipitation in Susquehanna Flats SAV beds. a**, Continuous measurements of DO% and pH from April to November 2016. The green shaded area represents the cruise period in August 2016. **b**, SEM images of $CaCO_3$ solids precipitated on the leaf surface of *V. americana*, collected in early September 2018. **c**, Mean ± s.d. ($n$ = 3–11) of the percentage of $CaCO_3$ content (% dry weight) for surface sediments and SAV leaves collected in early June and early September 2018.

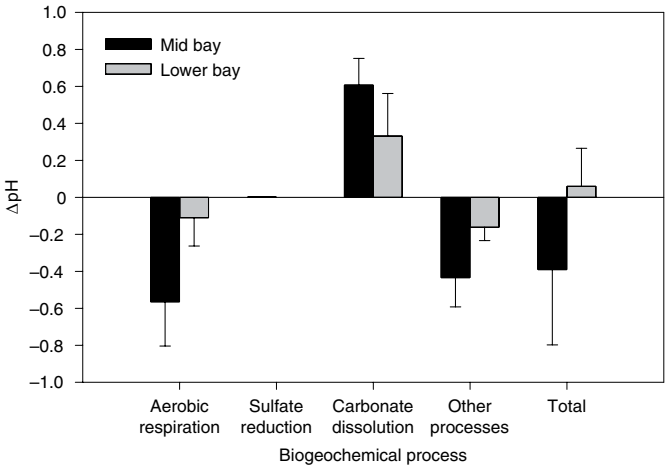


**Fig. 4 | Differential effects on pH from biogeochemical processes in the Chesapeake Bay.** Total non-conservative DIC and TA were decomposed into four components, including aerobic respiration, sulfate reduction, carbonate dissolution and other processes, such as sediment–water and air–water exchange. Differences between the pH calculated from measured DIC and TA and the new pH calculated without a component process are defined as ΔpH. Total is the sum of pH deviations induced by all processes. ΔpH (mean ± s.d.) was computed for the mid bay (black) and lower bay (grey).

were visually removed during pre-treatments of solid samples, the measured $CaCO_3$% is a minimum and represents the SAV-driven $CaCO_3$ formation excluding the shell calcification within the SAV beds. However, small shells could usually be found in the leaf and sediment samples. For example, the live clams collected on a recent cruise during August 2019 had a mean length of 1.38 ± 0.08 cm and a mean density of 338 ± 61 counts per $m^2$ in the flats. Thus, we conclude that the photosynthesis-induced high-pH and -$\Omega_{arag}$ environments could promote abiotic $CaCO_3$ precipitation and biogenic calcification within the SAV beds, leading to the observed decrease of $Ca^{2+}$ and TA in the tidal freshwater flats.

## Calcium carbonate dissolution in the mid to lower bay

In August 2016, the subsurface waters of the mid bay were characterized by low or no oxygen, low pH and $\Omega_{arag}$, and high $p_{CO_2}$ (Fig. 1b,g,h)—a condition favouring carbonate mineral dissolution. To better quantify the amount of $CaCO_3$ dissolution in the mid and lower bay, we adopted another two-endmember mixing scheme between stations CB2.2 (around salinity 5 in the upper bay) and AO1 (bay mouth) (Fig. 2a,b,d). Aerobic respiration and carbonate dissolution accounted for 72–81% of DIC addition in the subsurface water of the mid and lower bay (Supplementary Fig. 2). However, from the mid bay to lower bay, the intensity of all biogeochemical processes decreased. As aerobic respiration declined faster than the other three processes across this gradient, its percentage contribution to non-conservative DIC decreased from 33 to 14%, while the contributions of $CaCO_3$ dissolution and other processes increased from 47 and 19% to 58 and 28%, respectively. As the main process producing TA, $CaCO_3$ dissolution substantially increased the acid-buffering capacity of subsurface water. Sulfate reduction was only moderate in the summer of 2016 (Supplementary Fig. 2), reflected by a lower concentration of $H_2S$ in bottom water (Fig. 1c) than was measured on previous cruises[8].

To quantify the contribution of each biogeochemical process to pH changes in subsurface waters of the mid bay, we subtracted the amount of DIC and TA altered by each process from the measured values to calculate a new pH. Then, we defined the difference between the pH calculated from measured DIC, TA and the new pH to be ΔpH contributed by this process. The ΔpH derived from $CaCO_3$ dissolution (0.61 ± 0.15) can nearly offset the portion altered by aerobic respiration (−0.57 ± 0.24), while other processes, such as sediment–water exchange and air–water exchange, lower the pH by −0.43 ± 0.16 units relative to the conservative mixing (Fig. 4). If there were no $CaCO_3$ dissolution in the subsurface water of the mid bay, the pH would decrease by up to ~0.6 units more, which is substantially larger than the pH drawdown (~0.1 units) expected from anthropogenic $CO_2$-induced ocean acidification. Such a strong buffer effect may closely relate to the long water residence time of ~180 d (ref. [37]) and strong water stratification during summer in the Chesapeake Bay, which prevent the rapid vertical or horizontal dilution of the TA and buffering capacity produced from $CaCO_3$ dissolution[6].

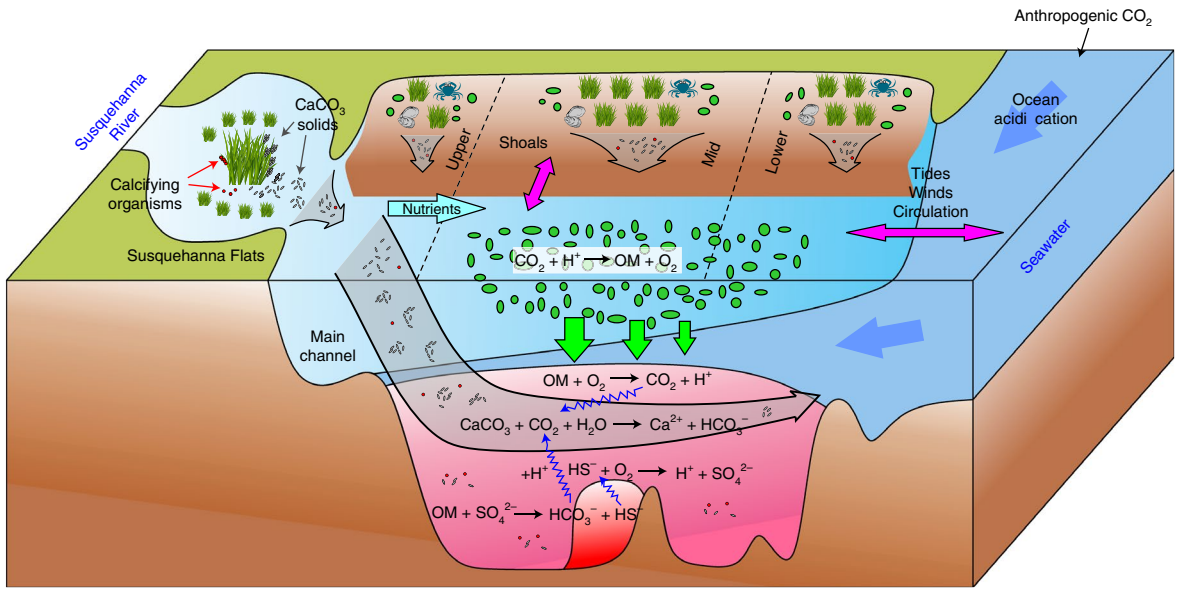


**Fig. 5 | Conceptual model of the self-regulated pH-buffering mechanism in the Chesapeake Bay.** Calcium carbonate is formed within the high-pH SAV beds in shallow waters, where it could be subsequently transported longitudinally and/or laterally into the deep main channel of the mid and lower bay and, upon dissolution, increases the pH-buffering capacity and alleviates coastal acidification (see main text for details). The chemical species involved are calcium carbonate ($CaCO_3$), carbon dioxide ($CO_2$), hydrogen ions ($H^+$), organic matter (OM), oxygen ($O_2$), water ($H_2O$), calcium ions ($Ca^{2+}$), bicarbonate ($HCO_3^-$), hydrogen sulfide ($HS^-$) and sulfate ($SO_4^{2-}$).

## A bay-wide self-regulated pH-buffering mechanism

Using an effective concentration method to correct the estuarine mixing effect[38,39], we quantified that, relative to the river endmember, at least 85% of TA removal by $CaCO_3$ formation at a salinity of <10 was subsequently released back by $CaCO_3$ dissolution at a salinity of ~10–22 (Extended Data Fig. 4). The amount of TA removal in excess of addition in the mesohaline main channel thus indicates the uncompensated removal signal from the upper bay as well as possible local $CaCO_3$ formation in the shallow waters. The local $CaCO_3$ supply may come from the extensive SAV beds and the calcification by relatively abundant mollusks[11,31,32], crustaceans[40] and foraminifera[41] along the shores in the mid bay and lower bay. Beyond a salinity of 22, the effective concentrations or removal percentages of TA and $Ca^{2+}$ become stable with a fractional loss of only 13 ± 10% and 2 ± 9%, respectively, relative to river input, indicating overall that the Chesapeake Bay is a weak TA and $Ca^{2+}$ sink, and has a nearly balanced internal cycle of $CaCO_3$. In other words, the newly produced $CaCO_3$ in the upper bay and shallow nearshore areas might have all dissolved to buffer the pH decrease in the subsurface mid and lower bay, resulting in only a small or nearly no net TA removal in the entire bay in late summer.

Our September 2018 survey in the Susquehanna Flats supports that aquatic biogeochemistry in the shallow, nearshore areas could be notably different from that in the main channel[42] (Extended Data Fig. 2). The $CaCO_3$ formation in the shallow areas and $CaCO_3$ dissolution in the subsurface water in the main channel are spatially decoupled, and there must be some physical transport processes linking these two important components of the carbonate cycle. As we do not have direct evidence to reveal the $CaCO_3$ transport unequivocally, we propose possible linkages as hypotheses to be further tested. In the longitudinal direction (for example, from the Susquehanna Flats to the mid bay), $CaCO_3$ precipitated on SAV leaf surfaces could probably reach the mid bay if it were fine-grained with a slow settling rate. Without considering the trapping effect by the SAV beds, our model simulation showed that small particles (diameter < 2 μm) released on the Susquehanna Flats could be transported downstream and reach the mid bay within 10 d, and had increasing impacts on the mid to lower bay from July to August (Extended Data Fig. 5). In addition, $CaCO_3$ particles may also be laterally transported over a smaller distance from shallow, nearshore areas to the main channel via frequent resuspension and deposition during wind events[43–45]. While $CaCO_3$ transport across adjacent systems and subsidized dissolution have been suggested previously[21,46], the details of the physical transport mechanisms for $CaCO_3$ solids require further research.

In addition to being a source of $CaCO_3$ solids, SAV could also buffer against eutrophication via particle trapping and nutrient assimilation and/or denitrification enhancement[29,47,48]. For instance, during our September 2018 sampling, nitrate concentrations in the flats were 2.2 ± 2.7 μM compared with 95 μM in the Susquehanna River. Meanwhile, DIN at the sites below flats was also substantially lower than that at the river mouth, indicating that this scavenging effect on DIN may extend beyond the SAV beds[49].

These results led us to propose a bay-wide self-regulated pH-buffering mechanism responding to coastal eutrophication and modulating acidification in a large bay (Fig. 5). With nutrient load reductions, the resurgent, dense SAV beds in the shallow parts of the Chesapeake Bay greatly elevate pH and $\Omega$ in the surrounding water, especially in the microzones on the leaf surface, stimulating the formation of $CaCO_3$ solids on leaf surfaces. These solids can be subsequently transported into the deep, oxygen-deficient zones in the main channel of the mid and lower bay, where the $CaCO_3$ solids react with anthropogenic and metabolic $CO_2$ and increase TA, thus buffering pH declines. Moreover, nutrient reductions can have a multiplicative effect on acidification, by reducing the supply of nutrients to support respiration-induced acidification outside the SAV beds in the main channel and simultaneously promoting SAV recovery that could further promote $CaCO_3$ formation therein. This self-regulated pH-buffering mechanism may also be observed in other coastal environments that are experiencing mitigation of eutrophication, reduction of phytoplankton primary production, resurgence of calcifying organisms and restricted water exchange with the open ocean. For instance, Abril et al.[10] demonstrated that the authigenic $CaCO_3$ precipitated in the Loire River was closely coupled with intense

primary production. Meanwhile, $CaCO_3$ dissolution occurred in the oxygen-deficient estuarine turbidity maximum zone.

The recovery of SAV in the Chesapeake Bay is a success of management efforts targeting nutrient load reductions[25], and continued recovery should amplify SAV-induced improvements in water quality[50]. Many previous reports have highlighted positive feedbacks within SAV beds that amplify their growth through improving local growing conditions[26,49]. However, this study suggests that SAV can mediate pH conditions far beyond the habitats where they grow, greatly extending the potential ecosystem impacts of SAV. In other words, the SAV-driven pH-buffering mechanism is an additional, unanticipated benefit of nutrient management efforts. These results show that coastal ecosystems can further promote their own recovery in complex, sometimes unpredictable ways as humans reduce anthropogenic stressors by ecosystem management. This positive feedback to coastal restoration can shed light on eutrophication and acidification studies in coastal systems emerging with recovery signs.

## Online content

Any methods, additional references, Nature Research reporting summaries, source data, extended data, supplementary information, acknowledgements, peer review information; details of author contributions and competing interests; and statements of data and code availability are available at https://doi.org/10.1038/s41561-020-0584-3.

Received: 17 January 2019; Accepted: 29 April 2020;
Published online: 1 June 2020

## References

1. Gattuso, J.-P. et al. Contrasting futures for ocean and society from different anthropogenic $CO_2$ emissions scenarios. *Science* **349**, aac4722 (2015).
2. Feely, R. A. et al. The combined effects of acidification and hypoxia on pH and aragonite saturation in the coastal waters of the California current ecosystem and the northern Gulf of Mexico. *Cont. Shelf Res.* **152**, 50–60 (2018).
3. Fabry, V. J., Seibel, B. A., Feely, R. A. & Orr, J. C. Impacts of ocean acidification on marine fauna and ecosystem processes. *ICES J. Mar. Sci.* **65**, 414–432 (2008).
4. Cai, W.-J. et al. Acidification of subsurface coastal waters enhanced by eutrophication. *Nat. Geosci.* **4**, 766–770 (2011).
5. Wallace, R. B., Baumann, H., Grear, J. S., Aller, R. C. & Gobler, C. J. Coastal ocean acidification: the other eutrophication problem. *Estuar. Coast. Shelf Sci.* **148**, 1–13 (2014).
6. Andersson, A. J., Mackenzie, F. T. & Lerman, A. Coastal ocean and carbonate systems in the high $CO_2$ world of the Anthropocene. *Am. J. Sci.* **305**, 875–918 (2005).
7. Macreadie, P. I., Serrano, O., Maher, D. T., Duarte, C. M. & Beardall, J. Addressing calcium carbonate cycling in blue carbon accounting. *Limnol. Oceanogr. Lett.* **2**, 195–201 (2017).
8. Cai, W.-J. et al. Redox reactions and weak buffering capacity lead to acidification in the Chesapeake Bay. *Nat. Commun.* **8**, 369 (2017).
9. Green, M. A., Waldbusser, G. G., Reilly, S. L., Emerson, K. & O'Donnell, S. Death by dissolution: sediment saturation state as a mortality factor for juvenile bivalves. *Limnol. Oceanogr.* **54**, 1037–1047 (2009).
10. Abril, G., Etcheber, H., Delille, B., Frankignoulle, M. & Borges, A. V. Carbonate dissolution in the turbid and eutrophic Loire estuary. *Mar. Ecol. Prog. Ser.* **259**, 129–138 (2003).
11. Waldbusser, G. G., Powell, E. N. & Mann, R. Ecosystem effects of shell aggregations and cycling in coastal waters: an example of Chesapeake Bay oyster reefs. *Ecology* **94**, 895–903 (2013).
12. Ware, J. R., Smith, S. V. & Reaka-Kudla, M. L. Coral reefs: sources or sinks of atmospheric $CO_2$? *Coral Reefs* **11**, 127–130 (1992).
13. Borowitzka, M. A. & Larkum, A. W. D. Calcification in algae: mechanisms and the role of metabolism. *Crit. Rev. Plant Sci.* **6**, 1–45 (1987).
14. Chauvaud, L., Thompson, J. K., Cloern, J. E. & Thouzeau, G. Clams as $CO_2$ generators: the *Potamocorbula amurensis* example in San Francisco Bay. *Limnol. Oceanogr.* **48**, 2086–2092 (2003).
15. Warren, L. A., Maurice, P. A., Parmar, N. & Ferris, F. G. Microbially mediated calcium carbonate precipitation: implications for interpreting calcite precipitation and for solid-phase capture of inorganic contaminants. *Geomicrobiol. J.* **18**, 93–115 (2001).
16. Perry, C. T. et al. Fish as major carbonate mud producers and missing components of the tropical carbonate factory. *Proc. Natl Acad. Sci. USA* **108**, 3865–3869 (2011).
17. Borowitzka, M. A. Calcification in aquatic plants. *Plant Cell Environ.* **7**, 457–466 (1984).
18. Mazarrasa, I. et al. Seagrass meadows as a globally significant carbonate reservoir. *Biogeosciences* **12**, 4993–5003 (2015).
19. Enríquez, S. & Schubert, N. Direct contribution of the seagrass *Thalassia testudinum* to lime mud production. *Nat. Commun.* **5**, 3835 (2014).
20. Corlett, H. & Jones, B. Epiphyte communities on *Thalassia testudinum* from Grand Cayman, British West Indies: their composition, structure, and contribution to lagoonal sediments. *Sediment. Geol.* **194**, 245–262 (2007).
21. Koch, E. W. Sediment resuspension in a shallow *Thalassia testudinum* banks ex König bed. *Aquat. Bot.* **65**, 269–280 (1999).
22. Orth, R. J. & Moore, K. A. Chesapeake Bay: an unprecedented decline in submerged aquatic vegetation. *Science* **222**, 51–53 (1983).
23. Orth, R. J. et al. Long-term trends in submersed aquatic vegetation (SAV) in Chesapeake Bay, USA, related to water quality. *Estuaries Coasts* **33**, 1144–1163 (2010).
24. Orth, R. J., Batiuk, R. A., Bergstrom, P. W. & Moore, K. A. A perspective on two decades of policies and regulations influencing the protection and restoration of submerged aquatic vegetation in Chesapeake Bay, USA. *Bull. Mar. Sci.* **71**, 1391–1403 (2002).
25. Lefcheck, J. S. et al. Long-term nutrient reductions lead to the unprecedented recovery of a temperate coastal region. *Proc. Natl Acad. Sci. USA* **115**, 3658–3662 (2018).
26. Kemp, W. et al. Eutrophication of Chesapeake Bay: historical trends and ecological interactions. *Mar. Ecol. Prog. Ser.* **303**, 1–29 (2005).
27. Murphy, R. R., Kemp, W. M. & Ball, W. P. Long-term trends in Chesapeake Bay seasonal hypoxia, stratification, and nutrient loading. *Estuaries Coasts* **34**, 1293–1309 (2011).
28. Su, J. et al. Source partitioning of oxygen-consuming organic matter in the hypoxic zone of the Chesapeake Bay. *Limnol. Oceanogr.* https://doi.org/10.1002/lno.11419 (2020).
29. Gurbisz, C. & Kemp, W. M. Unexpected resurgence of a large submersed plant bed in Chesapeake Bay: analysis of time series data. *Limnol. Oceanogr.* **59**, 482–494 (2014).
30. Waldbusser, G. G., Steenson, R. A. & Green, M. A. Oyster shell dissolution rates in estuarine waters: effects of pH and shell legacy. *J. Shellfish Res.* **30**, 659–669 (2011).
31. Waldbusser, G. G., Voigt, E. P., Bergschneider, H., Green, M. A. & Newell, R. I. E. Biocalcification in the eastern oyster (*Crassostrea virginica*) in relation to long-term trends in Chesapeake Bay pH. *Estuaries Coasts* **34**, 221–231 (2011).
32. Schulte, D. M. History of the Virginia oyster fishery, Chesapeake Bay, USA. *Front. Mar. Sci.* **4**, 127 (2017).
33. Officer, C. B. in *Estuarine and Wetland Processes: With Emphasis on Modeling* (eds Hamilton, P. & Macdonald, K. B.) 65–114 (Springer, 1980).
34. Beer, D. D. & Larkum, A. W. D. Photosynthesis and calcification in the calcifying algae *Halimeda discoidea* studied with microsensors. *Plant Cell Environ.* **24**, 1209–1217 (2001).
35. Semesi, I. S., Beer, S. & Björk, M. Seagrass photosynthesis controls rates of calcification and photosynthesis of calcareous macroalgae in a tropical seagrass meadow. *Mar. Ecol. Prog. Ser.* **382**, 41–47 (2009).
36. Koch, E. W. Hydrodynamics, diffusion-boundary layers and photosynthesis of the seagrasses *Thalassia testudinum* and *Cymodocea nodosa*. *Mar. Biol.* **118**, 767–776 (1994).
37. Du, J. & Shen, J. Water residence time in Chesapeake Bay for 1980–2012. *J. Mar. Syst.* **164**, 101–111 (2016).
38. Officer, C. B. Discussion of the behaviour of nonconservative dissolved constituents in estuaries. *Estuar. Coast. Mar. Sci.* **9**, 91–94 (1979).
39. Cai, W.-J., Wiebe, W. J., Wang, Y. & Sheldon, J. E. Intertidal marsh as a source of dissolved inorganic carbon and a sink of nitrate in the Satilla River–estuarine complex in the southeastern U.S. *Limnol. Oceanogr.* **45**, 1743–1752 (2000).
40. Heck, K. L. & Orth, R. J. Structural components of eelgrass (*Zostera marina*) meadows in the lower Chesapeake Bay—decapod crustacea. *Estuaries* **3**, 289–295 (1980).
41. Karlsen, A. W. et al. Historical trends in Chesapeake Bay dissolved oxygen based on benthic foraminifera from sediment cores. *Estuaries* **23**, 488–508 (2000).
42. Kemp, W. M., Smith, E. M., Marvin-DiPasquale, M. & Boynton, W. R. Organic carbon balance and net ecosystem metabolism in Chesapeake Bay. *Mar. Ecol. Prog. Ser.* **150**, 229–248 (1997).
43. Malone, T. C. et al. Lateral variation in the production and fate of phytoplankton in a partially stratified estuary. *Mar. Ecol. Prog. Ser.* **32**, 149–160 (1986).
44. Valle-Levinson, A. & Lwiza, K. M. M. The effects of channels and shoals on exchange between the Chesapeake Bay and the adjacent ocean. *J. Geophys. Res. Oceans* **100**, 18551–18563 (1995).

45. Fugate, D. C., Friedrichs, C. T. & Sanford, L. P. Lateral dynamics and associated transport of sediment in the upper reaches of a partially mixed estuary, Chesapeake Bay, USA. *Cont. Shelf Res.* **27**, 679–698 (2007).
46. Saderne, V. et al. Role of carbonate burial in Blue Carbon budgets. *Nat. Commun.* **10**, 1106 (2019).
47. Gruber, R. K. & Kemp, W. M. Feedback effects in a coastal canopy-forming submersed plant bed. *Limnol. Oceanogr.* **55**, 2285–2298 (2010).
48. Cafrey, J. M. & Kemp, W. M. Influence of the submersed plant, *Potamogeton perfoliatus*, on nitrogen cycling in estuarine sediments. *Limnol. Oceanogr.* **37**, 1483–1495 (1992).
49. Gurbisz, C. et al. Interactive effects of physical and biogeochemical feedback processes in a large submersed plant bed. *Estuaries Coasts* **40**, 1626–1641 (2017).
50. Orth, R. J. et al. Submersed aquatic vegetation in Chesapeake Bay: sentinel species in a changing world. *BioScience* **67**, 698–712 (2017).

## Methods

**Site and cruise descriptions.** During 8–12 August 2016, we cruised from the upper bay (CB2.1) southwards to the bay mouth (AO1) and back to the mid bay (CB5.3) (Extended Data Fig. 1). We revisited station 858C four times, CB4.3 and CB5.1 three times and CB5.2 twice. On 7 June and 4 September 2018, we conducted two supplementary surveys first upstream along the western channel, and then downstream across the SAV beds in the Susquehanna Flats (Extended Data Fig. 2).

**Sample and analytical methods.** Profiles of temperature, salinity and $O_2$ were acquired by YSI 6600, which was attached to a submerged pump. According to the bottom depth and the state of mixing, we pumped water from 2–7 depths to the deck for sampling. All samples were filtered using cellulose acetate cartridge filters (pore size: 0.45 µm), as recommended by Bockmon and Dickson[51] for reliable carbonate chemistry measurements in productive coastal environments. Salinities were double checked in discrete samples using a Cole-Parmer salinity meter. The DIC samples were preserved in 250-ml borosilicate glass bottles with 50 µl saturated $HgCl_2$ solution[52], but TA samples were not poisoned as HgS will precipitate out and $H^+$ will be released in anoxic waters[8,53,54]. Some efforts were made to avoid the possible alteration of TA during storage and analysis, including: (1) sample filtration to effectively remove all zooplankton, most of the phytoplankton and bacteria[55]; (2) keeping samples at low temperature (<4 °C) to minimize the biological activity; (3) shortening the sample storage time by analysing samples overnight (<24 h) and rarely over the next day (<36 h); and (4) keeping the duration of TA analysis (<10 min) short compared with the oxidation of sulfide or ammonia by oxygen. Time-delay measurements on replicate filtered and un-poisoned TA samples from the Susquehanna River were performed to confirm that biological alteration was minor (within the TA measurement precision ±2 µmol kg$^{-1}$) even after a 13-d delay in TA measurement. In addition, the measured TA values agreed well with TA values calculated from measured DIC and pH via CO2SYS, although the mean measured TA was significantly higher (~11 µmol kg$^{-1}$) than the mean calculated TA (paired *t*-test; $P<0.05$). Most of the TA differences (measured – calculated) were within ±20 µmol kg$^{-1}$ and did not correlate with the concentrations of $H_2S$ or $NH_4^+$, which could be explained by the contribution from organic alkalinity in the estuary, as well as the uncertainties of glass electrode pH measurements and the dissociation constants $K_1$ and $K_2$ of carbonic acid used in the calculation[56–59]. For DIC, a 1-ml sample was acidified and the extracted $CO_2$ gas was subsequently quantified with an infrared $CO_2$ detector (AS-C3 DIC Analyzer)[52]. All TA samples were analysed within 36 h of collection using Gran titration in an open-cell setting (AS-ALK2 Analyzer)[60]. The overall precision for DIC and TA was ±0.1%. Both DIC and TA measurements were calibrated against certified reference materials provided by A. G. Dickson at the Scripps Institution of Oceanography, University of California, San Diego.

The pH samples were measured on board using an Orion ROSS glass electrode within 1 h after the water temperature was stabilized at 25 °C in a thermal waterbath. The electrode was calibrated against three National Institute of Standards and Technology (NIST) standards (that is, 4.01, 7.00 and 10.01). Note that in the pH simulation, pH was also calculated from measured DIC and TA on the NIST scale via a modified version of the CO2SYS program that includes $H_2S$ and $NH_4^+$ in the acid–base equilibrium calculation[61], which agrees well with the measured pH (Supplementary Fig. 3). The $p_{CO_2}$ was also calculated via the CO2SYS program. Discrete dissolved oxygen samples were analysed by direct spectrophotometry of total iodine following Pai at al.[62] with a precision of ±1 µmol kg$^{-1}$. The $H_2S$ samples were measured using the spectrophotometric method following Fonselius at al.[63] with a precision better than 2.0%. $Ca^{2+}$ was measured using a modified technique of Kanamori and Ikegami[64] with a precision better than 0.1%. The $\Omega_{arag}$ was derived using measured $Ca^{2+}$, calculated $CO_3^{2-}$ and aragonite solubility, based on Mucci[65].

In the Susquehanna Flats (39.5056° N, 76.0413° W), temperature, salinity, dissolved oxygen, pH, turbidity and chlorophyll data were obtained by in situ sensors. The sensors were deployed between April and October within the SAV beds, and maintained by the Maryland Department of Natural Resources (http://www.eyesonthebay.net). The sensors were either YSI 6600 Extended Deployment Systems or YSI EXO2 model sondes, which were equipped with anti-fouling technology. SAV coverage data in the year 2016 were obtained from the dataset of SAV in Chesapeake Bay and Coastal Bays (http://web.vims.edu/bio/sav/SegmentAreaTable.htm).

During the field surveys in the Susquehanna Flats in September 2018, surface water samples of DIC, TA and $Ca^{2+}$ were taken at all sites, and solid samples of surface sediments and SAV leaves were collected in parts of sites in the shallow eastern flats. The solid samples were dried at 60 °C for 48 h. The microstructures and chemical composition of solids on the leaf surface were investigated using a focused ion beam and field emission scanning electron microscope (FIB-SEM, Zeiss AURIGA 60) equipped with an X-ray energy-dispersive spectrometer (Oxford Instruments; X-Max 80). After picking out the visible shells and epiphyte organisms, the solid samples were grounded for the determination of the percentages of $CaCO_3$ content (percentage dry weight) using thermal conductivity detector gas chromatography, generally following Stainton[66]. The coefficient of variation for the gas chromatography method used was ±3.3%.

**Determination of the endmembers and mixing lines.** We adopted two mixing schemes to distinguish the apparent carbonate alterations in different geographic scales. On a bay-wide scale, we used the mixing line between the Susquehanna River endmember and the offshore seawater endmember to discuss $CaCO_3$ formation and related biogeochemical dynamics (Fig. 2a). For the river endmember, historical datasets of chemical concentration and discharge rate were compiled, including DIC and TA from the laboratory of W.-J.C. during August 2015 to April 2017 ($n=35$ for DIC; $n=35$ for TA) and from the United States Geological Survey (USGS; site number 01578310) during January 1996 to June 2017 ($n=236$ for DIC; $n=246$ for TA), and $Ca^{2+}$ data from USGS (site number 01578310) during November 1978 to June 2017 ($n=435$), with the daily discharge rate $Q$ from USGS (site number 01578310). Then, we obtained linear relationships of DIC or TA or $Ca^{2+}$ with log[Q] (DIC = −524 × log[Q] + 2,695; $R^2=0.61$; $n=271$; $P<0.0001$; TA = −530 × log[Q] + 2,642; $R^2=0.62$; $n=281$; $P<0.0001$; $Ca^{2+}$ = −298 × log[Q] + 1,487; $R^2=0.69$; $n=435$; $P<0.0001$) (Supplementary Fig. 4). Finally, we derived the river endmember of DIC, TA and $Ca^{2+}$ from the specific discharge rate during the cruise period and 10 d previously[67]. The errors were propagated from the uncertainties of slope and intercept of the linear regression and of the specific freshwater discharge based on Taylor's expression[68]. Although the discharge varied by 27% over time during the cruise and multiple days before the cruise, it had little influence on the river endmember values (<5%) (Supplementary Table 2), which were within the uncertainties (Supplementary Table 1). For the offshore seawater endmember, we first made linear regressions of DIC or TA or $Ca^{2+}$ with salinity (DIC = 79 × salinity − 596; $R^2=0.72$; $P<0.0001$; TA = 54 × salinity + 428; $R^2=0.99$; $P<0.0001$; $Ca^{2+}$ = 269 × salinity + 831; $R^2=0.98$; $P<0.0001$) with data from four stations (82, 83, 85 and 87) in the Mid-Atlantic Bight, which were visited during the East Coast Ocean Acidification cruise in July 2015. Then, we used the salinity of the ocean endmember (33.618 ± 0.139) from Cai et al.[8] to derive the offshore endmember values.

To focus on $CaCO_3$ dissolution and related biogeochemical variations in the mid to lower bay, we adopted another mixing line between the southern end of the upper bay and the bay mouth (Fig. 2a). CB2.2 was considered to be a good endmember because waters upstream of CB2.2 were well mixed at this narrow section and no major tributary inputs were there. AO1 was another good endmember, because this station was just outside the bay mouth and its water column was thoroughly mixed with a maximum vertical salinity difference of 0.3. Further considering the sensitivity of $Ca^{2+}$ against salinity, we adopted the values of low-salinity layer (surface) at CB2.2 and high-salinity layer (bottom) at AO1 as endmembers. All of the endmember values and uncertainties are summarized in Supplementary Table 1.

**Calculation of total non-conservative DIC, TA and $Ca^{2+}$.** Regarding salinity as a conservative tracer, we calculated the mixing fractions between river water and seawater for each sample using equations (1) and (2):

$$f_R + f_{SW} = 1 \quad (1)$$

$$S_R \times f_R + S_{SW} \times f_{SW} = S_{meas} \quad (2)$$

where $S$ represents salinity, $f$ is the mixing fraction, the subscripts R and SW denote the river and seawater endmember, respectively, and meas represents the measured value. These fractions were applied to predict conservative concentrations of certain chemical constituents [$X$] (that is, DIC, TA or $Ca^{2+}$), resulting solely from two-endmember mixing:

$$[X]_{con} = [X]_R \times f_R + [X]_{SW} \times f_{SW} \quad (3)$$

The difference (Δ[$X$]) between measured and conservative values represents the total non-conservative value of [$X$] caused by several biogeochemical processes:

$$\Delta[X]_{non\_c} = [X]_{meas} - [X]_{con} \quad (4)$$

where the subscripts non_c and con stand for non-conservative and conservative, respectively.

**Quantifying biogeochemical processes in the upper bay.** In the upper bay, we separated the total non-conservative [$X$] (DIC or TA) into four components:

$$\Delta[X]_{non\_c} = \Delta[X]_{AR} + \Delta[X]_{CP} + \Delta[X]_{OG} + \Delta[X]_{sedi} \quad (5)$$

where the subscripts AR, CP, OG and sedi denote aerobic respiration, $CaCO_3$ precipitation, $CO_2$ outgassing and sediment–water exchange, respectively. There was no sulfate reduction in the upper bay. Sediment–water exchange includes porewater exchange with scale lengths of millimetres to metres and submarine groundwater discharge (SGD) with scale lengths of metres to kilometres, which may be comparable in magnitude in some coastal regions[69]. In the Chesapeake Bay, SGD input was found near the head of the bay and in some tributaries, but the SGD rate was estimated to be much smaller than the riverine flux of freshwater to the bay (<10%)[70,71]. Considering that carbonate parameters within SGD have not been reported in the Chesapeake Bay, it is difficult to further quantify the relative contributions of porewater exchange versus SGD to the DIC and TA flux from the sediment. By considering the chemical stoichiometry involved in different

biogeochemical processes[8], we can use apparent oxygen utilization (AOU), $\Delta Ca^{2+}$ and $p_{CO_2}$ (calculated from measured DIC and TA) to quantify $\Delta[X]_{AR}$, $\Delta[X]_{CP}$ and $\Delta[X]_{OG}$. As shown in Supplementary Fig. 1, we first simulated the proportion of non-conservative DIC or TA caused by aerobic respiration and $CaCO_3$ precipitation, which are marked as yellow crosses (DIC) and yellow plus signs (TA). Then, we computed the residence time at subdomains of CB2.1 (39.40–39.45° N) and CB2.2 (39.30–39.40° N) by simple volume/volumetric flow rate. Through equation $\Delta DIC_{OG} = \frac{flux \times \tau}{H}$ (where flux is the $CO_2$ flux calculated from $p_{CO_2}$, $\tau$ indicates the residence time and $H$ is the average water depth), we could calculate the proportion of non-conservative DIC caused by $CO_2$ outgassing (cyan arrows in the inset in Supplementary Fig. 1). Note that air–water $CO_2$ exchange does not influence TA. $\Delta[X]_{sedi}$ (DIC or TA) is calculated as a residue in equation (5) and thus includes all DIC and TA fluxes from multiple processes in sediments including porewater exchange and SGD.

Nutrient changes may also affect TA due to the nutrient $H^+$ compensation principle[72,73]. First, our approach directly uses the deviation from the mixing line or the non-conservative part of $Ca^{2+}$ concentration to estimate $CaCO_3$ formation and dissolution, thus it does not require nutrient correction. Second, since $NH_4^+$ and $NO_2^- + NO_3^-$ were measured at each station and each depth during the cruise in August 2016, the changes of nutrients could be quantified using two-endmember mixing calculations. Note that only the non-conservative part of nutrient change contributes to TA change and the nutrient concentration change due to dilution by river–ocean mixing does not. The results showed that $NH_4^+$ was generally produced, while $NO_2^- + NO_3^-$ was consumed, both leading to TA increase within the bay. In a bay-wide mixing scenario (river–offshore), the TA increase caused by $NH_4^+$ production and $NO_2^- + NO_3^-$ consumption ranged from 15–37 μmol kg$^{-1}$ in the low-salinity zone (salinity < 10), which was relatively small compared with TA removal in the upper bay (~500–700 μmol kg$^{-1}$). Therefore, we did not perform nutrient corrections for TA, and mathematically those nutrient-related TA changes could be attributed to the residual term of the TA mass balance equation (equation (5)) (that is, $\Delta TA_{sedi}$), which was thought to be mainly affected by sediment processes.

**Quantifying biogeochemical processes and the pH changes in the mid to lower bay.** For the subsurface water in the mid to lower bay, we divided the total non-conservative [$X$] (DIC or TA) into four components:

$$\Delta[X]_{non\_c} = \Delta[X]_{AR} + \Delta[X]_{SR} + \Delta[X]_{CD} + \Delta[X]_{others} \quad (6)$$

where the subscripts AR, SR, CD and others denote aerobic respiration, sulfate reduction, $CaCO_3$ dissolution and other processes, respectively. Following Cai et al.[8], we used AOU, $H_2S$ and $\Delta Ca^{2+}$ to quantify $\Delta[X]_{AR}$, $\Delta[X]_{SR}$ and $\Delta[X]_{CD}$. Then, $\Delta[X]_{others}$ was calculated as the residue of the above equation, which was mainly influenced by sediment–water exchange, as well as air–water exchange (Supplementary Fig. 2). Note that in a regional mixing scenario (CB2.2-AO1), the average value of nutrient-related TA increase is 13 ± 12 μmol kg$^{-1}$, which only accounts for ~5 ± 5% of the total non-conservative TA addition (231 ± 73 μmol kg$^{-1}$). Thus, we did not correct nutrient changes for TA, and mathematically, those nutrient-related TA changes can be attributed to $\Delta TA_{others}$. To evaluate the extent to which each biogeochemical process affects pH in the subsurface water, we subtracted the amount of DIC and TA altered by each process from the measured values to calculate a new pH. Then, we defined the difference between the pH calculated from measured DIC and TA and the new pH to be ΔpH (Fig. 4).

**Evolution of DIC, TA and $Ca^{2+}$ at stations CB2.1 and CB2.2.** As shown in Supplementary Fig. 1, the combined effect of $CaCO_3$ precipitation and aerobic respiration drew down DIC by 345 μmol kg$^{-1}$ at CB2.1 and 333 μmol kg$^{-1}$ at CB2.2, followed by $CO_2$ outgassing, which lowered DIC by 202 μmol kg$^{-1}$ at CB2.1 and by 291 μmol kg$^{-1}$ at CB2.2. Sediment exchange elevated DIC by 18 μmol kg$^{-1}$ at CB2.1 and lowered DIC by 43 μmol kg$^{-1}$ at CB2.2 to reach the total non-conservative DIC of −529 μmol kg$^{-1}$ at CB2.1 and −667 μmol kg$^{-1}$ at CB2.2. Thus, $CO_2$ outgassing was enhanced by 89 μmol kg$^{-1}$ and sediment turned from a weak source to a weak sink from CB2.1 to CB2.2. Note that $CO_2$ outgassing could not influence TA. Similarly, the synergy of carbonate precipitation and aerobic respiration drew down TA by 773 μmol kg$^{-1}$ at CB2.1 and 768 μmol kg$^{-1}$ at CB2.2, followed by sediment exchange, which elevated TA by 250 μmol kg$^{-1}$ at CB2.1 and 85 μmol kg$^{-1}$ at CB2.2 to reach the total non-conservative TA of −523 μmol kg$^{-1}$ at CB2.1 and −683 μmol kg$^{-1}$ at CB2.2. Thus, sediment exchange was weakened by 165 μmol kg$^{-1}$ from CB2.1 to CB2.2. The evolution of DIC, TA and $Ca^{2+}$ indicates that $CaCO_3$ precipitation plays a vital role in the carbonate dynamics in the upper bay. In addition, high spatial variability of biogeochemical processes exists in the upper bay, where the water column is well mixed and the water flow is relatively high.

**Model simulation on $CaCO_3$ particle transport.** The sediment resuspension in the SAV beds is typically lower than in the unvegetated area, because SAV beds can reduce the current velocity and attenuate wave energy, and thus decrease sediment erosion and enhance particle deposition[74]. However, when the water depth is larger than the maximum meadow height, wave attenuation is less efficient, and sediment is deposited as well as resuspended[75]. In addition, the geomorphology of the SAV beds (for example, the Susquehanna Flats) is spatially complex and characterized by unvegetated patches and shallow channels through the SAV beds. Water flow can be diverted around and between vegetation patches, increasing current velocities and associated near-bottom shear stresses and thus promoting non-deposition and/or erosion[76]. The flow intensification near the bottom can possibly cause higher total suspended solid levels in the vegetated area (featured by fine particles) than in the unvegetated area (featured by coarser particles) at low wave energy[21]. It can be expected that sediment resuspension within SAV beds would be even higher under stronger tidal currents or episodic high wind events[77], which frequently affect the Chesapeake Bay. The particle transport pathways over SAV beds are not clear so far, and may be a function of river discharge, winds, topography, vegetation, proximity to channels/SAV bed edges and hydrodynamic gradients similar to particle transport in marshes[78–80]. It is beyond the scope of our study to simulate the particle transport over SAV beds.

Without considering the trapping effect by the SAV beds, we conducted a model simulation on the transport of $CaCO_3$ particles in 2016 using a sediment module incorporated into the Regional Ocean Modeling System[81]. Particles with three different sizes (that is, 2, 8 and 20 μm) and settling velocities were released at all water depth (20 layers) on the Susquehanna Flats on 31 May 2016 at 00:00. Particle deposition, resuspension of deposited sediment and sea bed erosion were considered in this simulation. Our model results show that the fine-grained particles (diameter = 2 μm) from the Susquehanna Flats could reach the mid bay within 10 d, and had increasing impacts on the mid to lower bay from July to August (Extended Data Fig. 5). The medium-sized particles with a diameter of 8 μm could also reach the upper parts of the mid bay within 10 d, but had less impact on the mid and lower bay in the following 2 months (data not shown). Particles with a diameter of 20 μm were mostly trapped in the upper bay throughout the summer (data not shown). The model results support that the fine-grained $CaCO_3$ solids such as those precipitated on the SAV leaf surface could probably be transported over a long distance to the main channel of the mid to lower bay. Although this numerical model simulation does help to depict a 'what if' given that the fine particles can escape the SAV beds, further studies are needed to reveal how particles could be transported out of the SAV beds and to provide more details on the longitudinal and lateral transport mechanisms along the main channel.

## Data availability

The data presented in this study can be found in the NCEI Ocean Archive with accession number 0209358. Source data are provided with this paper.

## References


51. Bockmon, E. E. & Dickson, A. G. A seawater filtration method suitable for total dissolved inorganic carbon and pH analyses. *Limnol. Oceanogr. Methods* **12**, 191–195 (2014).
52. Huang, W. J., Wang, Y. & Cai, W. J. Assessment of sample storage techniques for total alkalinity and dissolved inorganic carbon in seawater. *Limnol. Oceanogr. Methods* **10**, 711–717 (2012).
53. Goyet, C., Bradshaw, A. L. & Brewer, P. G. The carbonate system in the Black Sea. *Deep Sea Res. A* **38**, S1049–S1068 (1991).
54. Hiscock, W. T. & Millero, F. J. Alkalinity of the anoxic waters in the Western Black Sea. *Deep Sea Res. II* **53**, 1787–1801 (2006).
55. Verdugo, P. et al. The oceanic gel phase: a bridge in the DOM–POM continuum. *Mar. Chem.* **92**, 67–85 (2004).
56. Cai, W.-J., Wang, Y. & Hodson, R. E. Acid–base properties of dissolved organic matter in the estuarine waters of Georgia, USA. *Geochim. Cosmochim. Acta* **62**, 473–483 (1998).
57. Millero, F. J. Carbonate constants for estuarine waters. *Mar. Freshwater Res.* **61**, 139–142 (2010).
58. Hunt, C. W., Salisbury, J. E. & Vandemark, D. Contribution of non-carbonate anions to total alkalinity and overestimation of $pCO_2$ in New England and New Brunswick rivers. *Biogeosciences* **8**, 3069–3076 (2011).
59. Yang, B., Byrne, R. H. & Lindemuth, M. Contributions of organic alkalinity to total alkalinity in coastal waters: a spectrophotometric approach. *Mar. Chem.* **176**, 199–207 (2015).
60. Cai, W.-J. et al. Alkalinity distribution in the western North Atlantic Ocean margins. *J. Geophys. Res. Oceans* **115**, C08014 (2010).
61. Xu, Y.-Y., Pierrot, D. & Cai, W.-J. Ocean carbonate system computation for anoxic waters using an updated CO2SYS program. *Mar. Chem.* **195**, 90–93 (2017).
62. Pai, S. C., Gong, G. C. & Liu, K. K. Determination of dissolved oxygen in seawater by direct spectrophotometry of total iodine. *Mar. Chem.* **41**, 343–351 (1993).
63. Fonselius, S., Dyrssen, D. & Yhlen, B. in *Methods of Seawater Analysis* (eds Grasshoff, K. et al.) 91–100 (Wiley, 2007).
64. Kanamori, S. & Ikegami, H. Computer-processed potentiometric titration for the determination of calcium and magnesium in sea water. *J. Oceanogr. Soc. Japan* **36**, 177–184 (1980).

65. Mucci, A. The solubility of calcite and aragonite in seawater at various salinities, temperatures, and one atmosphere total pressure. *Am. J. Sci.* **283**, 780–799 (1983).
66. Stainton, M. P. A syringe gas-stripping procedure for gas-chromatographic determination of dissolved inorganic and organic carbon in fresh water and carbonates in sediments. *J. Fish. Res. Board Can.* **30**, 1441–1445 (1973).
67. Joesoef, A., Kirchman, D. L., Sommerfield, C. K. & Cai, W.-J. Seasonal variability of the inorganic carbon system in a large coastal plain estuary. *Biogeosciences* **14**, 4949–4963 (2017).
68. Taylor, J. R. *An Introduction to Error Analysis* Ch. 3 (University Science Books, 1997).
69. Hong, Q., Cai, P., Shi, X., Li, Q. & Wang, G. Solute transport into the Jiulong River estuary via pore water exchange and submarine groundwater discharge: new insights from $^{224}$Ra/$^{228}$Th disequilibrium. *Geochim. Cosmochim. Acta* **198**, 338–359 (2017).
70. Hussain, N., Church, T. M. & Kim, G. Use of $^{222}$Rn and $^{226}$Ra to trace groundwater discharge into the Chesapeake Bay. *Mar. Chem.* **65**, 127–134 (1999).
71. Luek, J. L. & Beck, A. J. Radium budget of the York River estuary (VA, USA) dominated by submarine groundwater discharge with a seasonally variable groundwater end-member. *Mar. Chem.* **165**, 55–65 (2014).
72. Brewer, P. G. & Goldman, J. C. Alkalinity changes generated by phytoplankton growth. *Limnol. Oceanogr.* **21**, 108–117 (1976).
73. Wolf-Gladrow, D. A., Zeebe, R. E., Klaas, C., Körtzinger, A. & Dickson, A. G. Total alkalinity: the explicit conservative expression and its application to biogeochemical processes. *Mar. Chem.* **106**, 287–300 (2007).
74. Fonseca, M. S. in *Estuarine Shores: Evolution, Environments and Human Alterations* (eds Nordstrom, K. & Roman, C. T.) 261–286 (Wiley, 1996).
75. Ward, L. G., Michael Kemp, W. & Boynton, W. R. The influence of waves and seagrass communities on suspended particulates in an estuarine embayment. *Mar. Geol.* **59**, 85–103 (1984).
76. Russ, E. R. & Palinkas, C. M. Seasonal-scale and decadal-scale sediment-vegetation interactions on the subaqueous Susquehanna River Delta, Upper Chesapeake Bay. *Estuaries Coasts* **41**, 2092–2104 (2018).
77. Gurbisz, C., Kemp, W. M., Sanford, L. P. & Orth, R. J. Mechanisms of storm-related loss and resilience in a large submersed plant bed. *Estuaries Coasts* **39**, 951–966 (2016).
78. Marani, M. et al. On the drainage density of tidal networks. *Water Resour. Res.* **39**, 1040 (2003).
79. Temmerman, S., Bouma, T. J., Govers, G. & Lauwaet, D. Flow paths of water and sediment in a tidal marsh: relations with marsh developmental stage and tidal inundation height. *Estuaries* **28**, 338–352 (2005).
80. D'Alpaos, A., Lanzoni, S., Marani, M. & Rinaldo, A. Landscape evolution in tidal embayments: modeling the interplay of erosion, sedimentation, and vegetation dynamics. *J. Geophys. Res. Earth Surf.* **112**, F01008 (2007).
81. Xie, X., Li, M. & Ni, W. Roles of wind-driven currents and surface waves in sediment resuspension and transport during a tropical storm. *J. Geophys. Res. Oceans* **123**, 8638–8654 (2018).


## Acknowledgements

This work was supported by grants from the US National Oceanic and Atmospheric Administration (NA15NOS4780184, NA15NOS4780190 and NA18NOS4780179). We acknowledge the USGS, Maryland Department of Natural Resources and Virginia Institute of Marine Science (VIMS) for the monitoring data. We thank C. Hodgkins for assistance with the field work. This is University of Maryland Center for Environmental Science publication number 5821 and reference number UMCES CBL 2020-101.

## Author contributions

W.-J.C. was responsible for the design of the work. J.S. analysed the data. B.C. and J.M.T. co-led the cruises. B.C., J.S., J.B., N.H., K.M.S. and Y.-Y.X. were responsible for sample collection and analysis. Y.Y. and C.N. contributed to the mineralogical analysis. M.L., X.X. and W.N. contributed to physical mixing and particle transport. J.C. and M.S.O. contributed to the weight percentage of $CaCO_3$. J.M.T., C.G. and G.G.W. contributed supplementary materials and data. J.S. and W.-J.C. drafted the manuscript. All authors contributed to discussion and revision of the manuscript.

## Competing interests

The authors declare no competing interests.

## Additional information

**Extended data** is available for this paper at https://doi.org/10.1038/s41561-020-0584-3.

**Supplementary information** is available for this paper at https://doi.org/10.1038/s41561-020-0584-3.

**Correspondence and requests for materials** should be addressed to W.-J.C.

**Peer review information** Primary Handling Editors: James Super; Xujia Jiang.

**Reprints and permissions information** is available at www.nature.com/reprints.

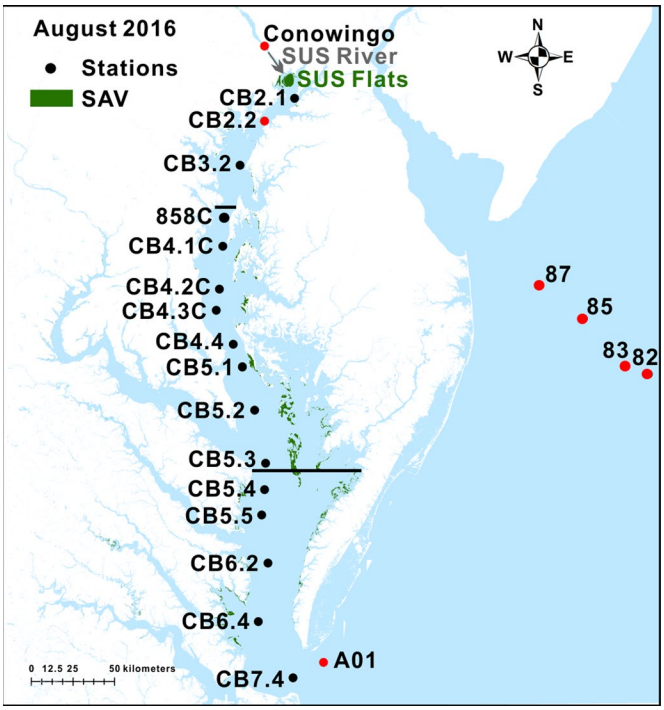


**Extended Data Fig. 1 | Sampling sites during August 2016 cruise in the Chesapeake Bay.** Green areas show the coverage of Submersed Aquatic Vegetation (SAV) beds in the Chesapeake Bay in 2016 (http://www.vims.edu/bio/sav/maps.html). The upper, mid and lower bay (separated by the black lines) accounted for 16.4%, 64.0% and 19.6% of the total SAV coverage in 2016 (39,524 hectares). The arrow shows the outlet of the Susquehanna River. Red circles show the related locations of the four endmembers. Note that stations 82, 83, 85 and 87 are located further offshore in the Mid-Atlantic Bight and were visited during July 2015.

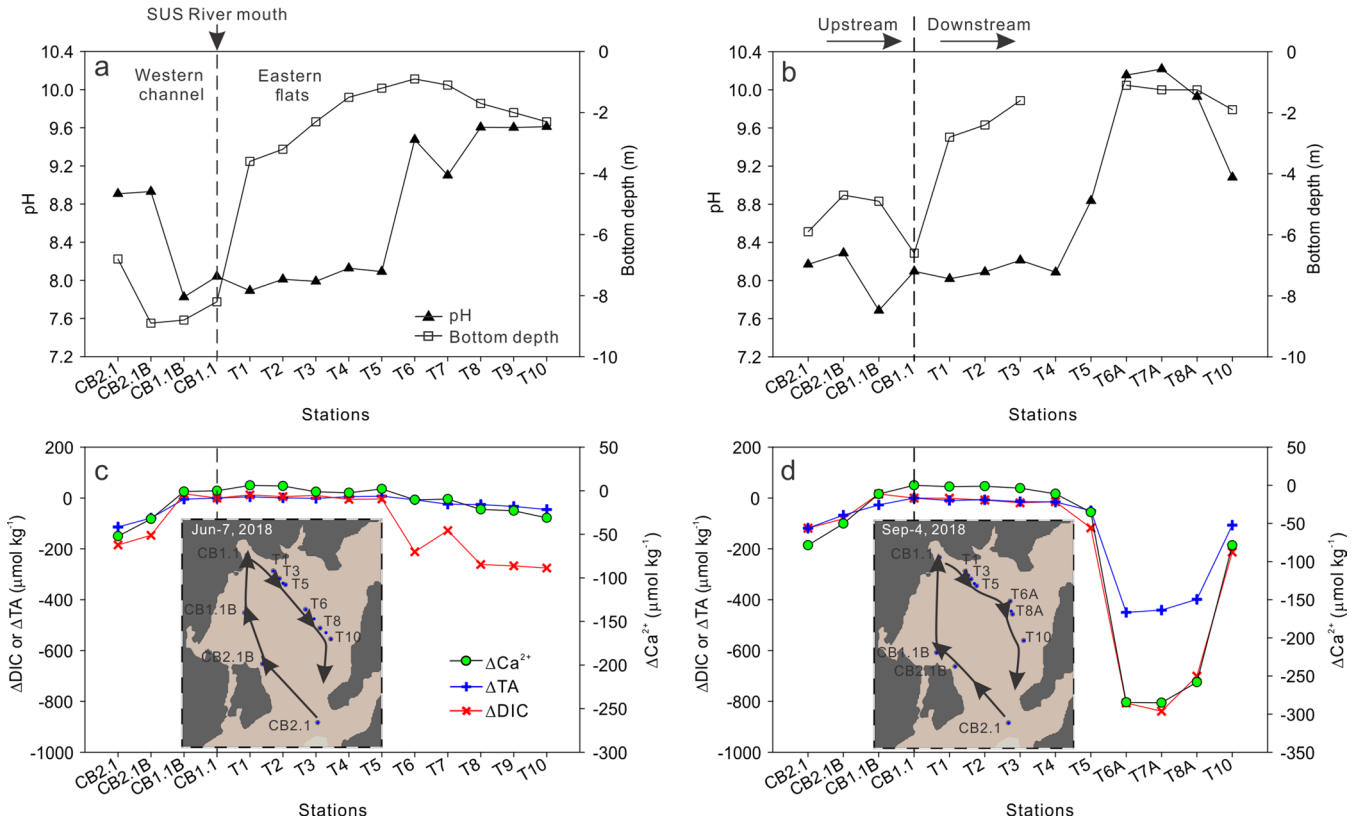


**Extended Data Fig. 2 | Carbonate system variations and bottom depths in the vicinity of the Susquehanna Flats in 2018.** The dashed line separates the western deep channel and eastern shallow flats, where SAV beds were present. The arrows show the cruise path. Sampling sites are labelled in the inserted maps. The SAV biomass was low in early June (**a**, **c**), but was high in early September (**b**, **d**) 2018. The Δ values in each station are relative to CB1.1, which was our uppermost station near the Susquehanna River mouth.

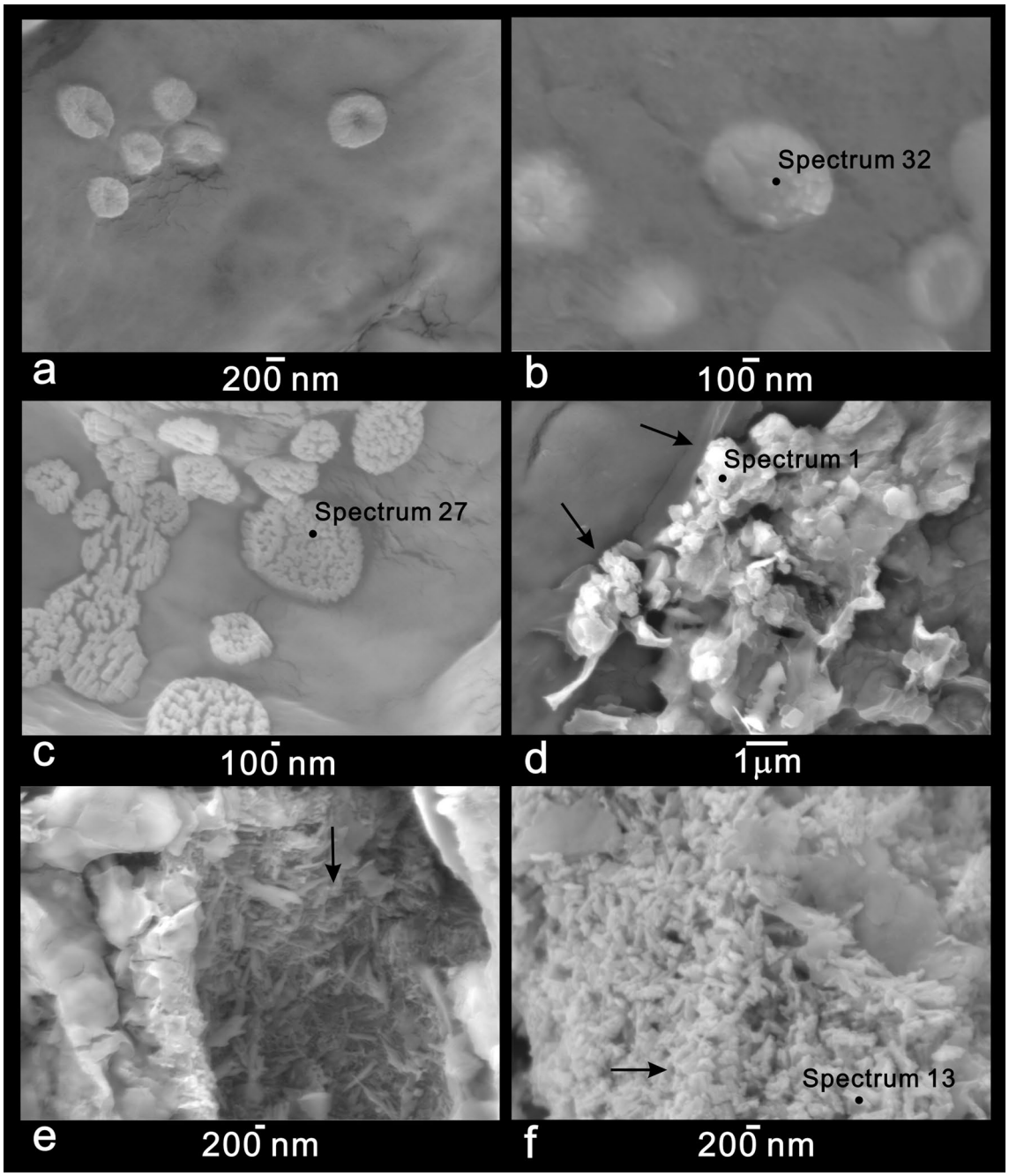


**Extended Data Fig. 3 | SEM images of $CaCO_3$ precipitates on the leaf surface of *Vallisneria americana* collected from Susquehanna Flats in 2018.** **a**, semi-spherical crystallites; **b**, ellipsoidal crystallites; **c**, polycrystalline maze-like aggregates; **d**, aggregates with other materials; **e**, arborisation-like aggregates; **f**, rice-like aggregates. The atomic composition in Spectrum 32: 41.8% C, 18.4% Ca, 17.2% O, 10.5% K, 6.5% C, 1.9% Na, 1.6% S, 1.3% Mg, 0.8% P; Spectrum 27: 40.8% C, 25.2% O, 14.4% Ca, 9.2% N, 5.3% K, 2.4% Mg, 1.6% P, 1.0% Na; Spectrum 1: 42.9% O, 27.7% Ca, 25.4% C, 1.4% K, 1.2% Si, 0.9% Al, 0.2% Na, 0.2% Mg; sum spectrum in (e): 31.1% C, 29.9% O, 22.3% Ca, 4.6% Fe, 4.4% Si, 3.8% Al, 2.0% K, 1.9% Mg; Spectrum 13: 41.6% O, 38.1% Ca, 12.5% C, 3.7% K, 1.5% Cl, 1.1% Mg, 0.9% Si, 0.5% Na, 0.2% Al.

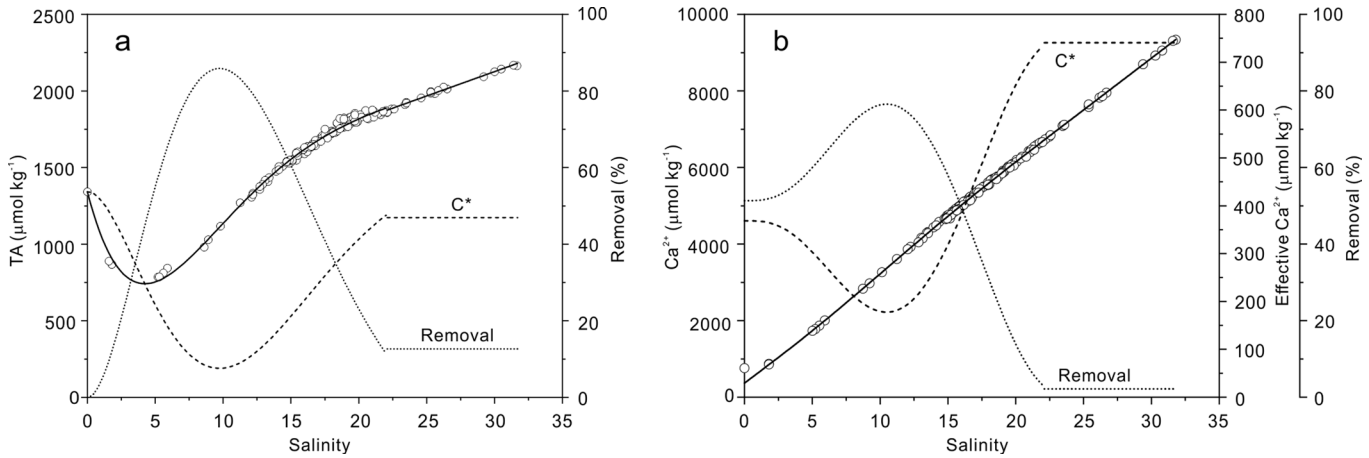


**Extended Data Fig. 4 | Effective concentration (C˙) and removal (percentage) of TA and $Ca^{2+}$ in the Chesapeake Bay in August 2016.** The fitting equation for TA (**a**) at salinity <=22 is C = 0.00002708×$S^6$-0.00336738×$S^5$+0.17376067×$S^4$-4.6574875×$S^3$+64.65219917×$S^2$-344.24526458×$S$+1342.095396, whereas at salinity >22 the equation is C = 31.791176×$S$ +1172.4787872. The fitting equation for $Ca^{2+}$ (**b**) at salinity <=22 is C = -0.00001835×$S^6$+ 0.00171504×$S^5$-0.05591518×$S^4$+0.67310609×$S^3$-0.73633157×$S^2$+265.9022229×$S$+368.4115086, while at salinity >22 the equation is C = 270.483366×$S$ + 740.833973. C˙ can be acquired by extending the derivative at any salinity to zero salinity in a concentration-salinity plot. The removal percentage at any salinity relative to freshwater input can be calculated via removal (%) = ($C_0$-C˙)/$C_0$×100, where $C_0$ means the concentration at freshwater end.

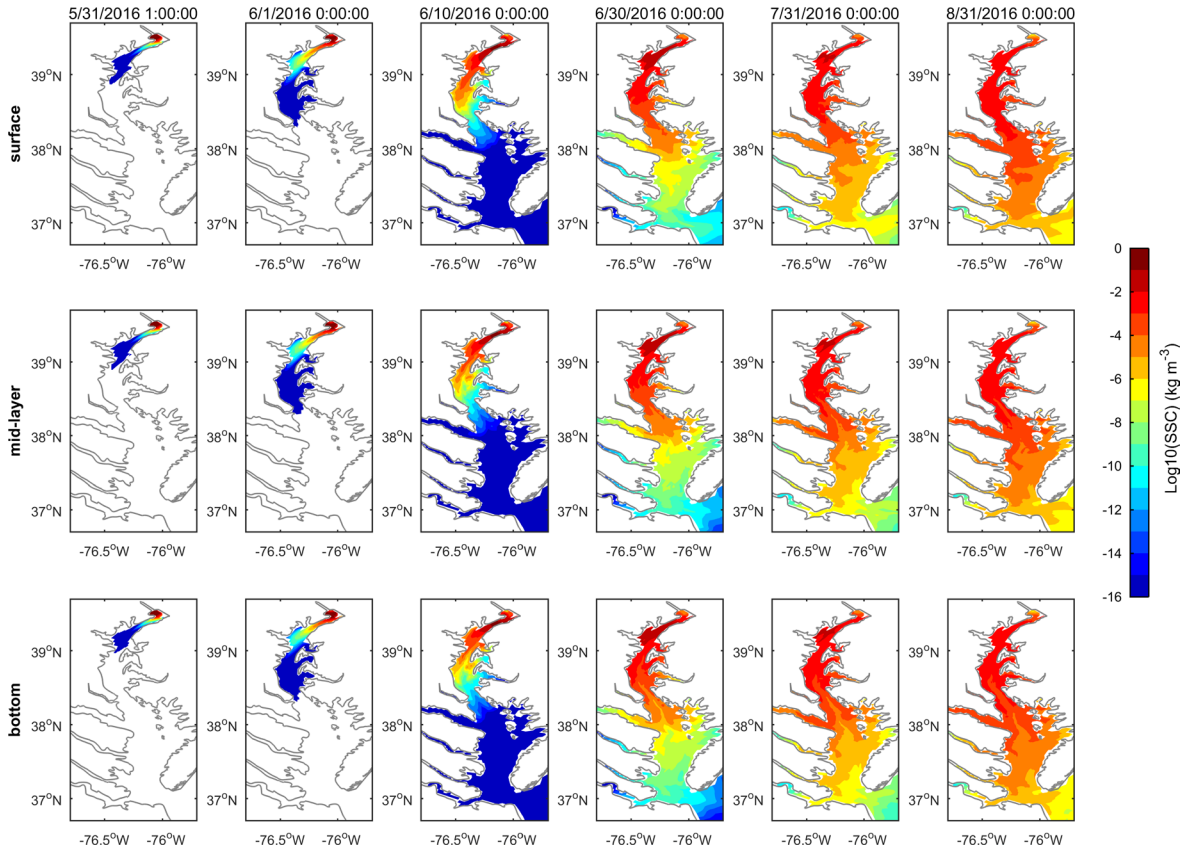


**Extended Data Fig. 5 | Numerical model simulation of the transport of fine particles from the Susquehanna Flats in the Chesapeake Bay.** The model simulates suspended sediment concentration (SSC) at surface, mid-depth and bottom water in the bay after the initial release of sediment particles (diameter = 2 μm) from all water depths on the Susquehanna Flats. SSC is shown on a logarithmic scale. The initial concentration is set as 0.5 kg $m^{-3}$ over the Susquehanna Flats and the release time is on 00:00:00 May 31$^{th}$, 2016. The output snapshots are the concentrations 1 hour, 1 day, 10 days, 30 days, 60 days and 90 days after the initial release of particles.